Version of Record: https://www.sciencedirect.com/science/article/pii/S138718111930335X
Manuscript_80150fc2939355fc3fc423bdf26b0bf2

Carbide derived carbon obtained from SiC-based fibers by phosphating-NaOH bath process

*Stéphane Mazerat, Joséphine Lacroix, René Pailler**

University of Bordeaux, Laboratoire des Composites ThermoStructuraux, UMR 5801 (CNRS - UB - Groupe SAFRAN - CEA), 3 allée de la Boetie, 33600 Pessac, France

* Corresponding author. Tel +33 5 56 84 47 33; Fax +33 5 56 84 12 25. E-mail: pailler@lcts.u-bordeaux.fr

Carbide derived carbon (CDC) are unique materials with tunable micro and mesopore size distribution. They are produced selectively removing metallic elements from carbides. Halogenation or hydrothermal treatments were, therefore, extensively studied. The study reports a new route to produce such carbon, aforementioned CDCp, applied to SiC-based fibers by reacting phosphoric acid vapors at 580–800 °C range, followed by condensed silicophosphate dissolution in tempered NaOH bath. Fibers could be, this way, fully or partially transformed. Obtained CDCp show a broad pore size distribution extending from microporosity (7–9 Å) to mesoporosity (up to 60 Å), specific surface area >1000 $m^2 g^{-1}$ and pore volume >0.7 $cm^3 g^{-1}$. Mesoporosity may infer from partial carbon oxidation or *in-situ* silicophosphate and carbon demixion at nanoscale. CDCp burn-off kinetics and tensile strength of non-etched fiber core are discussed. Depending on phosphating conditions, monolayer or concentric CDCp tubes could coat each individual fiber within complex fabric geometry.

Keywords

SiC fiber . porous coating . phosphating etching . carbide derived carbon . silicophosphate

© 2019 published by Elsevier. This manuscript is made available under the Elsevier user license
https://www.elsevier.com/open-access/userlicense/1.0/

1. Introduction

Since their first apparition in the 70's, SiC-based fibers have been tremendously documented, based on great hopes to withstand severe condition applications, mostly high temperature under oxidative environment due to passive oxidation. They show good mechanical properties and heat resistance [1]; they can be woven to be used as ceramic matrix composite (CMC) reinforcement, structural parts with high toughness and damage tolerance [2]. These unique properties are given by PyC or BN chemical vapor infiltrated interphase material. Nevertheless, contacts between fibers are not eliminated with this route, leading to fiber failure by cluster: crack propagation from fiber to fiber. One identified solution consists in transforming the fiber surface itself into a crack deviating material, silicon or carbon based.

Silicon carbide etching has been extensively documented for electronic or micro-electro-mechanical systems. J.W. Faust reports possible SiC etching agents [3]. Among them, some consist in the elimination of both silicon and carbon atoms, such as physical treatment (ion beam…), wet etching in alkaline (NaOH, KOH…) or acids (HNO_3 + HF) [4]. Others are based on layer-by-layer extraction of silicon atoms from the lattice: physical treatment under plasma, chemical treatment under hot gases (Cl_2, F_2) [5,6] or liquid (diluted H_3PO_4) [7], thermal decomposition [8,9], or hydrothermal treatment [10–12]. Selective silicon etching results in the formation of carbide derived carbon (CDC) coating, material extensively studied after halogenation (chlorination) treatment [5,13]. It offers homogeneous amorphous carbon films [9,10] with attractive linear kinetics for thicknesses lower than 100 µm [14] at intermediate temperatures (400 < T < 1000 °C) and preserves the original carbide shape. Due to pore size control in sub-ångströmetric range (micro or mesopores), through substrate selection, treatment temperature, oxidation controlled chemical or physical activation

[15–23], CDC have been studied for supercapacitor, tribology, gas storage, adsorbents or catalysis applications. Such gaseous etching treatment could successfully transform the surface of individual SiC-based fibers in a homogeneous CDC coating [24] with well controlled thickness, despite woven tows geometry constraints [25]. Chlorination kinetics of such material were reported to be sensitive to oxygen content [22] as well as heteroelement type [26–31]. Moreover, a remarkable improvement of SiCO fiber tensile strength was reported after surface etching [32], phenomenon ascribed to critical surface flaws depletion after fractographic observations. The tensile strength improvement, together with its use as CVI-PyC alternative or use for impregnation of boron nitride precursor [33–35], have driven several works for application on lower cost CMC for civil aircraft jet engine [26].

Recently, an alternative etching route was tested on SiCO fibers by phosphoric acid vapors between 600 °C and 800 °C [28,36]. This treatment results in a homogeneous transformation of each fiber, within tows or woven, in carbon and silicophosphate rich layers according to the following reaction:

$$x\mathrm{SiC} + 2x\mathrm{H_2O} + y\mathrm{P_2O_5} = x\mathrm{C} + 2x\mathrm{H_2} + x\mathrm{SiO_2}.y\mathrm{P_2O_5} \text{ or } x\mathrm{SiP_2O_7} \text{ when } x = y \quad (1)$$

The phosphatation mechanism consists in silicon oxidation forming silica in which phosphorus pentoxide is dissolved. Depending on P_2O_5 amount, so formed silicophosphates was found under glass ($x\mathrm{SiO_2}.y\mathrm{P_2O_5}$ with $y \leq 0.3$) or crystalline ($\mathrm{SiP_2O_7}$) forms [37]. Because of its low solubility in glass, carbon is ejected as peripheral phase. This demixion reaction followed by coalescence could lead to lenticular, granular, mono or multilayered $(\mathrm{SiO_2}.\mathrm{P_2O_5}/\mathrm{carbon})_n$ morphologies. A further selective dissolution of condensed silicophosphate phases leaves a carbon skeleton. This SiC-based fibers etching process is, by the principle, similar to hydrothermal treatment [11,12], but separated in two steps: (i) selective oxidation of silicon with no elimination of carbon and (ii) dissolution of the silicon

oxide phase, leaving the carbon skeleton. Using P_2O_5 as a third agent helps to perform both stages at atmospheric pressure and intermediate temperatures. Carbon was not oxidized during the treatment because of (i). high phosphoric acid concentration used (Eq. (1)) (ii) low water vapor reaction with carbon in the chosen temperature range and (iii). the higher reducibility of silicon and phosphorus.

The objective of the present study was to isolate and characterize the carbon phase, aforementioned CDCp for carbide derived carbon via phosphating. Silicophosphate can be dissolved by hydrolysis in alkaline hydroxide bath [38] according to Eq. (2). KOH or NaOH are two possible alkaline hydroxides foreseen in this purpose, but also known as chemical activation agents above their melting temperature (360 °C and 318 °C respectively) [17,18,39–42]. Under aqueous form and temperature below 100 °C, such activation is however not likely to occur leaving untouched the carbon skeleton further characterized. Nevertheless, phosphoric acid, which is also a known chemical activation agent for carbon at temperature above 200 °C, should actively impact CDCp physical properties [43–45].

$$SiP_2O_7 + 3H_2O = SiO_2 + 2PO_4^{3-} + 6H^+ \quad (2)$$

The feasibility of such treatment was first studied through phosphating and subsequent dissolution kinetics assessment on Tyranno® Grade-S fibers. Different transformation morphologies could be achieved, depending on etching settings. A comparative study of the pore structure for both CDC, produced by phosphatation or chlorination [28–32] and applied to 5 different SiC-based fibers, is reviewed. Burn-off kinetics and mechanical properties, assessed by monofilament tensile tests, of so coated fibers are also presented.

2. Materials and experimental procedure

2.1 Materials

Silicon carbide fibers are synthesized by the conversion of a polymer derived ceramic (PDC), the polycarbosilane or derivate containing small amount of organometallic and commercialized by Nippon Carbon Co. Ltd. or UBE Industries Ltd. under the trade names Nicalon® or Tyranno®. First-generation fibers process consists in PDC melt spinning, then oxygen cured and pyrolyzed at 1200–1300 °C [46,47]. They are composed of a silicon oxycarbide phase (SiCO) embedding SiC grains in nanometer range and free aromatic carbon as basic structural units (Table 1). Second-generation fibers are electron beam cured and thus oxygen free, which increases their thermal stability above 1000 °C. Five (5) fibers were considered for this study, four (4) belongs to the first-generation Nicalon® NL207, Tyranno® Grade-S, Lox-M and ZMI and one (1) to the second-generation Hi-Nicalon®. Emphasis was put on the first-generation Grade-S fiber type, doped with titanium with an average diameter of 8.5 µm and approximately 1600 filament per tow, for its high chemical reactivity against aggressive environment [29,30] to highlight treatment settings impact. 2D woven tows were considered in the present study (200 x 20 mm) to have a representative sample mass.

Fiber	Diameter	Si	C	O	X	C_{free}	SiC	SiCO	C_{free}	Ø β-SiC
	(µm)	(at.%)					(vol.%)			(nm)
NL207	14	38.6	48.6	12.8	-	16.4	36	25	39	1.9
Grade-S	8.5	31.8	48.1	19.4	Ti: 0.7	26.0	19	27	54	1.2
Lox-M	11	35.4	53.3	10.4	Ti: 0.9	23.1	41	8	51	1.9
ZMI	11	35.5	54.3	10.0	Zr: 0.2	23.9	43	6	52	2.2
Hi-Ni	14	41.9	57.2	0.9	-	15.8	61	0	39	5.0

Table 1: Chemical composition, phase volume proportion and microstructure of the selected silicon carbide fibers [48]. Chemical composition was measured at CNRS facility in Solaize by ICP-AES and oxidation. The amount of crystallized β-SiC was determined by X-Ray diffraction (XRD) and the mean size (Ø β-SiC) assessed by the Scherrer formulae. The amount of SiCO infers from difference between chemical composition and quantity of β-SiC and C_{free}.

2.2 CDCp elaboration

Prior to any treatment, fabrics were desized at 650 °C for 10 min in air, followed by thin silica film removal in 10 vol.% hydrofluoric acid bath for 4 min. Phosphatation was operated in a dedicated device. The reaction took place at atmospheric pressure in a slit-shape graphite reactor (10 x 60 x 200 mm) inserted in a vertical silica tube with 70 mm diameter, itself protected from aggressive gases by graphite foil (Papyex® from Mersen Ltd.) and installed in a vertical 3-zones resistive furnace. A 30 mm long isothermal zone was ensured by 30 conical Papyex® thermal shields centrally perforated, placed above and below the reactor. Prior to heating-up, the system was evacuated using a foreline water-pump then filled with pure nitrogen carrier gas. Once the desired temperature reached (20 °C min^{-1} heating ramp), aqueous phosphoric acid (85wt.%, P_2O_5/H_2O = 1/5) was injected in dripping mode from the upper sleeve through a needle, falling into an alumina crucible placed in hot zone above the reactor to be vaporized. Acid injection rate was controlled by a peristaltic pump. Treatment temperature range was limited to 580–800 °C to avoid phosphate glass formation (lower limit) or carbon (reactor, CDCp) oxidation by water vapors (upper limit). No acid condensation was observed above the reactor, showing the efficiency of shields toward convection. A conical lower sleeve ensured the condensed vapors flowed in a 1 L empty washing bottle. Two other bottles, filled with water, further washed the gas. The system was quenched after a given duration by purging under 0.03 L s^{-1} nitrogen flow at 650 °C for one hour (evaporation of potential phosphate glass or condensates), pursuing during the subsequent cooling down.

Phosphated woven were thereafter treated in tempered and stirred 200 mL NaOH bath in order to dissolve silicophosphate phases. Samples were afterward washed in distilled water and dried at 120 °C for several hours. Hydrolysis kinetic, or dissolution rate, was assessed by

mass loss on 400 mg fabric samples. Transformation yields were not estimated after this synthesis method, because each step involved uncertainties in weight change (handling or stirring) biasing such calculation. So treated samples are here referred as CDCp followed by the treatment reference when Grade-S substrate was used or identified by the suffix "DCp", following the fiber type in other cases (CDCp-700 or NL207-DCp for instance). In the same manner, suffix "DC" was used to define CDC resulting from chlorination.

2.3 CDCp characterization

Morphological analyses were performed using scanning electron microscopy (SEM Hitachi S4500) at both manufacturing steps (prior to washing or after) on the section of a tow pulled out from the fabric. Five (5) fibers were randomly selected and transformation thickness (contrast detected) measured at five (5) locations on each. Chemical composition of coating was studied by EDS (FEI Quanta 400 FEG with EDAX GENESIS XM4i) performed on thin samples, ion milled with an ion slicer (JEOL) at 6 kV. Nature of crystal phase was identified by X-Ray diffraction (XRD Siemens D5000 θ-2θ).

Nitrogen adsorption analysis was carried out using a commercial Micromeretics ASAP 2010 at 77 K with a 10 s equilibration interval. Because of CDCp hygroscopic tendency, samples of 1 g were outgassed at 300 °C for twelve (12) hours under secondary vacuum. The equivalent specific surface area (SSA in $m^2 g^{-1}$) and the C parameter inferred from Brunauer-Emmett-Teller (BET) equation [49] for $P/P_0 < 0.35$. Effective micropore volume and size distribution (μ-PSD) were calculated using the semi-empirical Horvath-Kawazoe (H-K) approach [50] with slit pore geometry. The mesopore size distributions (meso-PSD) were calculated by Barrett-Joyner-Halenda (BJH) method [51] based on a modified Kelvin equation. This method account for partial pressures above 0.45 and pores larger than 40 Å. Volume of mesoporosity inferred from adsorption branch to limit cavitation-induced misestimation.

Single point total pore volume ($V_{p,0.99}$) was assessed using the Gurvich rule, determined from the specific amount of gas adsorbed at a relative pressure close to the saturation vapor pressure ($0.90 < P/P_0 < 0.99$), with a density conversion factor of 1.5468×10^{-3} cm^3 cm^{-3} (STP) [52,53].

Oxidation kinetics were studied by Thermo-Gravimetric Analysis (TAG 24, Setaram Inc.) under pure and dry oxygen flow (60 NmL min^{-1}) with a linear ramp of 5 °C min^{-1} until 650 °C. These tests were performed just after non-destructive nitrogen adsorption analysis on 50 mg samples, placed in an alumina crucible and outgassed under primary vacuum at room temperature for several minutes. This measured weight loss fraction could be considered to post-correct the sample mass for nitrogen physisorption experiment, assuming a non-porous fiber core, thus representing the only CDCp material characterization.

2.4 Tensile testing

Monofilament tensile tests were performed at ambient temperature and atmosphere on a dedicated device. 20 to 30 fibers were randomly pulled out from a central tow of the fabric, after alkaline hydroxide bath. Each fiber was mounted, aligned and Loctite® glued to a centrally opened (25 mm window) paper holder. The diameter of each sample inferred from their laser diffraction patterns, value later replaced by direct SEM measurement when fragment could be rescued. The paper holder was then gripped in the device. Prior to be cut, a layer of paraffin grease was deposited on probe. Tensile test was carried out at a constant elongation rate (0.5 % min^{-1}) measured by a LVDT mounted on the grips. Machine compliance was estimated, for elongation correction, performing ten more tests at 10 and 40 mm gauge lengths. Fragments were afterward washed in acetone, mounted on brass plate and SEM observed for diameter measurement and critical flaw type assessment. Critical flaw

position was revealed by the classical fragile rupture pattern (mirror, mist, hackle, branching). Strength statistic was interpreted using a single modal Weibull distribution, model inferred as follows:

$$P_i = 1 - e^{-\left(\frac{\sigma}{\sigma_0}\right)^m} \quad (3)$$

Where P_i is the probability of failure ($P_i = (i-0.5)/n$), n the number of values, σ the tensile strength, σ_0 the Weibull characteristic strength corresponding to the fiber volume for which 37% of the sample will survive and m the Weibull modulus.

3. Results

3.1 Phosphating-dissolution experiments

The phosphating transformation thickness evolves linearly with etching time in the 580–800 °C range following an Arrhenius law ($k = k_0\, e^{-Ea/RT}$) with k the transformation rate (nm s^{-1}), k_0 the pre-exponential factor, Ea the apparent activation energy (J mol^{-1}), R the universal gas constant (8.314 J mol^{-1} K^{-1}) and T the temperature (K). Apparent activation energy of Tyranno® Grade-S phosphating reaction was estimated to be 110 kJ mol^{-1} in the 600–700 °C range. For higher temperatures, the kinetic remained linearly related to etching duration (Fig. 1a), but no longer followed the Arrhenius law (Fig. 1b). This phenomenon was ascribed to the temperature-related fraction of diffusing oxygen which, above a given threshold, partly entraps phosphorus under its oxidized form (P_2O_5) in surface-located silicophosphate glass, hence limiting transformation kinetic. Three different phases result from this etching treatment: carbon rich phase, silicophosphate glass (10–30 mol.% P_2O_5) and silicon diphosphate (SiP_2O_7) crystals (Fig. 2) resulting from former glass devitrification [54,55]. Large crystals can be observed at fiber surface, where the quantity of phosphorus is

not limited. Silicon and phosphorus were undoubtedly identified in the carbon layer by EDS which suggests the presence of contaminating silicophosphate phase, further washed away (Fig. 2). These glass domains would either be entrapped or being transported to coalesce.

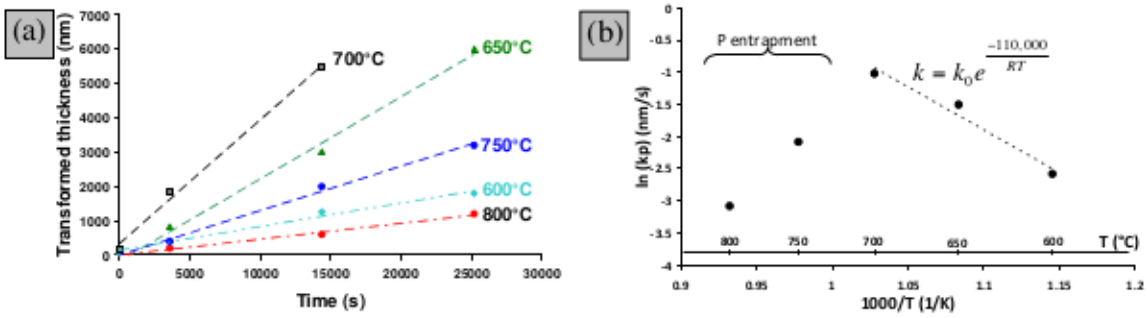

Fig. 1: Phosphating kinetics of Tyranno® Grade-S fiber, measured on tows for 7.3 x 10^{-2} and 83 NmL min^{-1} of phosphoric acid and nitrogen flows respectively, showing (a). the linear transformation rate and (b). Arrhenius diagram.

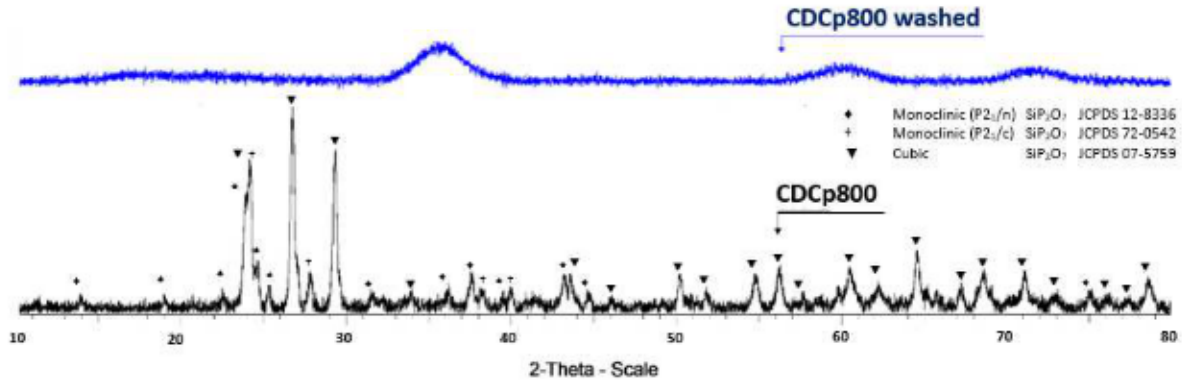

Fig. 2: X-ray diffraction pattern of phosphated SiC-based fibers (CDCp-800 conditions) before and after NaOH washing step.

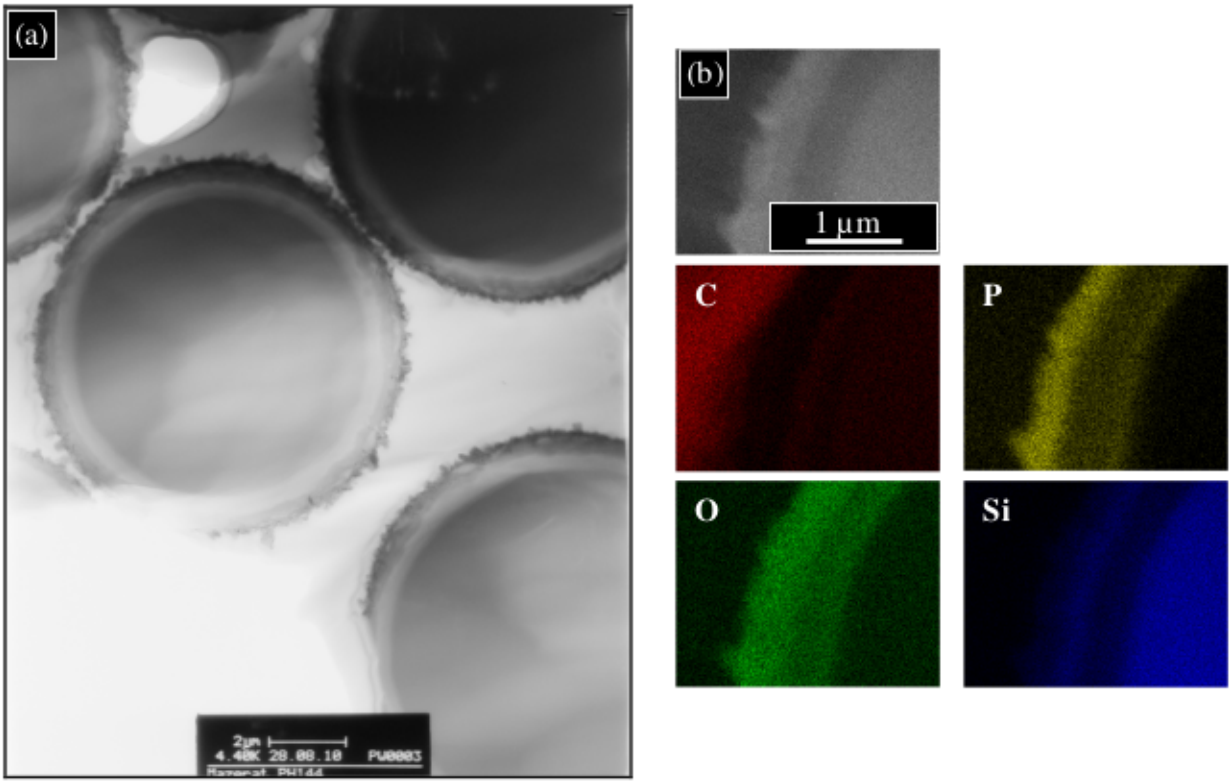

Fig. 3: (a). Bright-Field Transmission Electron Microscope characterization of a Si-C-O fiber (TS) phosphated at 700°C and (b). Energy dispersive X-ray spectroscopy mapping performed on the same sample (30 kV acceleration tension).

In Table 2, five phosphating conditions for Grade-S are summarized. They were chosen, based on previous parametric study [28], according to 3 objectives: (i). identify a possible effect of the etching temperature on CDCp properties, (ii). obtain layers about or exceeding one micrometer to guaranty non-negligible carbon coating mass and (iii). reach homogeneous transformation morphology for each fiber of the woven. The objective, here, is to obtained comparable and representative samples at various temperatures and consequently not to comment the effect of phosphating single factors (flow rate, duration) individually adjusted therefore. It is worth noting the transformation thickness objective could not be fulfilled with CDCp-580 conditions due to limited kinetics. Moreover, on fabric samples, the phosphoric acid and carrier gas (nitrogen) flows were increased to limit the reaction gradient among the

sample height, progressive reactant depletion, and ensure the third above mentioned objective. This explains the lower etching depth observed (Fig. 4). Even though, some variability was observed depending on the position of the observed tow in woven.

Sample	Temperature (°C)	Time (min)	Acid flow (mL min^{-1})	N_2 flow (NmL min^{-1})	CDCp thickness (nm)
CDCp-580	580	120	3.6×10^{-2}	450	130
CDCp-600	600	300	8.7×10^{-2}	250	800-1000
CDCp-700	700	420	2.2×10^{-1}	450	1000-2000
CDCp-800	800	240	7.3×10^{-2}	250	1000-2000
CDCp-tt	700	600	2.9×10^{-1}	83	-
NL207-DCp	700	240	7.3×10^{-2}	450	500
Lox-M-DCp	750	420	1.4×10^{-1}	250	800
ZMI-DCp	750	420	1.4×10^{-1}	250	800
Hi-Ni-DCp	700	240	7.3×10^{-2}	83	1000

Table 2: Experimental conditions for phosphating treatments of different SiC-based fibers. The firsts 5 lines refer to Grade-S fibers.

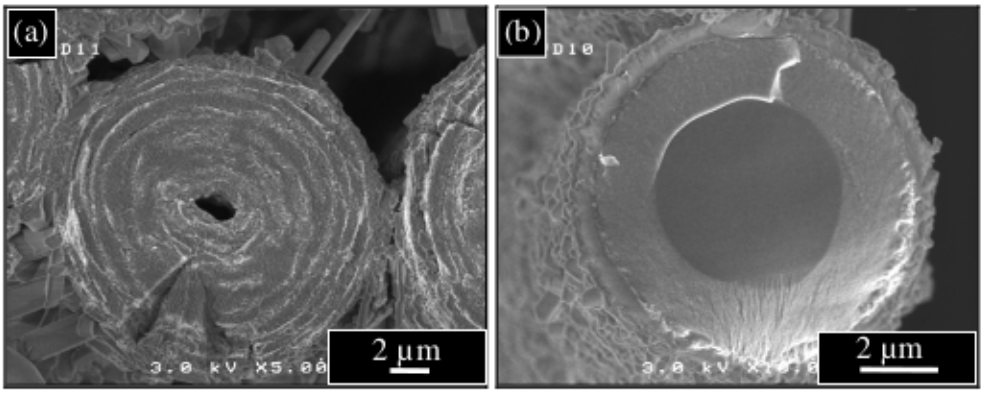

Fig. 4: Impact of the sample mass after a phosphating treatment (7 h 700 °C) on (a). single 30 mm long tow (7.3×10^{-2} mL min^{-1} acid and 83 NmL min^{-1} carrier gas flows) fully transformed or (b). 2D fabric 200 x 20 mm (2.2×10^{-1} mL min^{-1} acid and 450 NmL min^{-1} carrier gas flows) transformed on 2 µm depth, CDCp-700.

Fully transformed CDCp-tt samples seem to consist only on SiP_2O_7 crystals with carbon layers; the glassy phase was likely integrally devitrified (threshold of phosphorus content)

during the extended phosphating treatment duration (Fig. 5e–h). Therefore, former fiber shape is hardly recognized due to oxidation and devitrification-induced volume expansion. Some morphological discrepancies are observed between CDCp-600 and CDCp-700 or CDCp-800 samples. Indeed, even if the surface is always constituted of a glass/SiP_2O_7 layer, the under-layer consists in an alternated (carbon/glass)$_n$ layers in CDCp-600, whereas it is a carbon rich monolayer for higher temperatures (Fig. 5). This multilayer morphology was attributed to a spontaneous demixion of carbon and glass followed by coalescence of glass domains to limit surface energy. In the temperature range 600–650 °C this coalescence transportation would be limited to short distances leading to successive glass layers. For higher temperature however, transportation distance range would be enhanced, and glass domains could reach the fiber surface leading to larger glass/SiP_2O_7 shell (Fig. 5c–d). The multilayer morphology is neither observed at lower temperatures (Fig. 5a), presumably due to limited transformation thickness, lack of oxygen (low water vapor reactivity) or to non-thermally activated coalescence transportation.

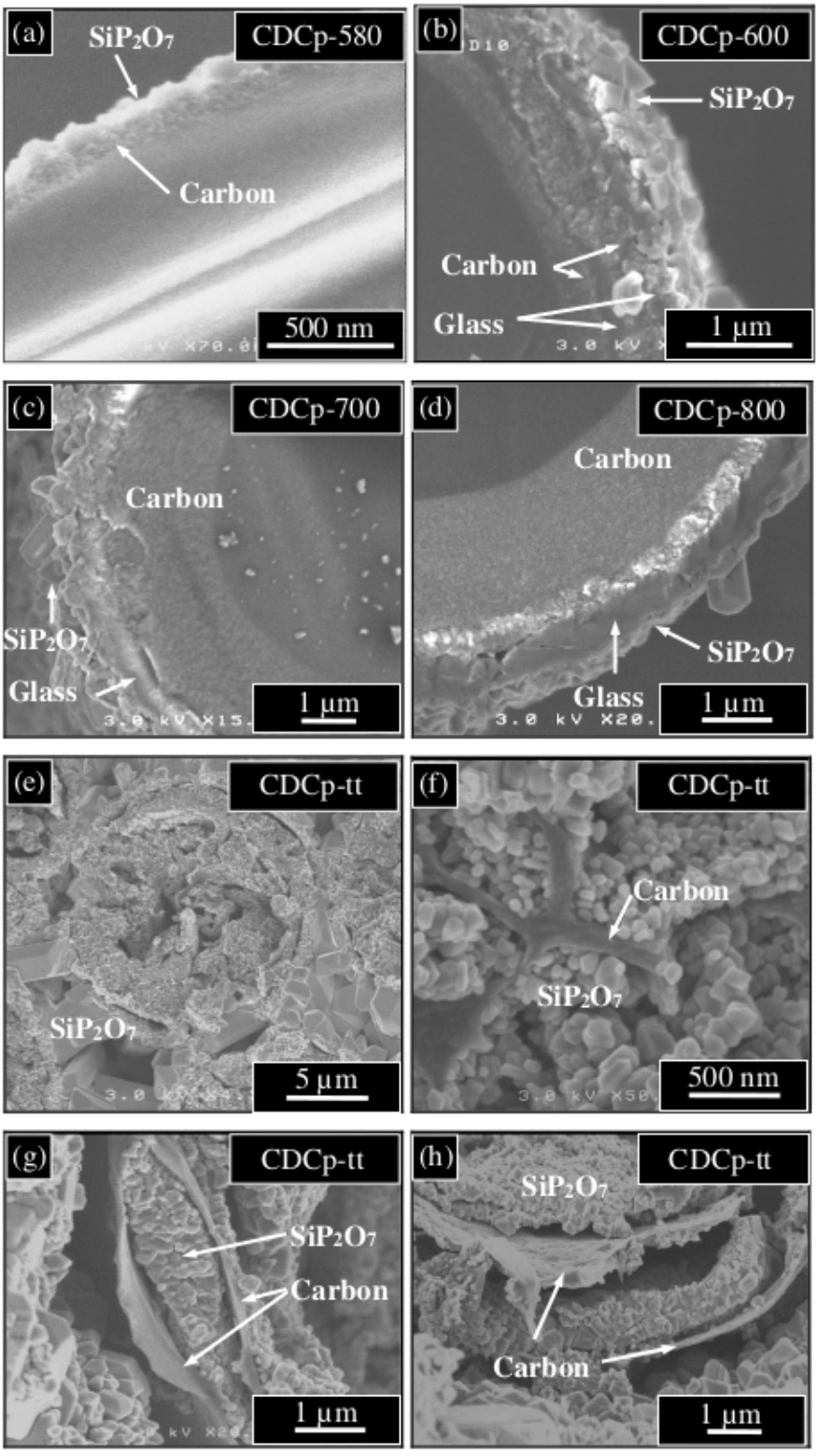

Fig. 5: SEM sectional morphology of phosphated Grade-S samples (a). CDCp-580, (b). CDCp-600, (c). CDCp-700, (d). CDCp-800 and (e–h). CDCp-tt.

Study of silicophosphate dissolution in NaOH solution was performed on intensively devitrified CDCp-800 sample. Preliminary trials highlighted washing can be separated in two distinct steps: (i). in early minutes of experiments glass was hydrolyzed whatever the sodium hydroxide concentration; (ii). for extended durations the dissolution of more stable silicon diphosphate (SiP_2O_7) occurred. This first step was not considered for this study, hence the use of CDCp-800. The weight loss is linearly related to bath duration until a threshold value (Fig. 6a) corresponding to complete dissolution as revealed by SEM, EDS and XRD analysis (Fig. 2). This observation, true for any treatment condition, confirms the selective silicophosphate dissolution treatment is effective and not altered by layered morphology (CDCp-600). It further indicates the kinetic is not piloted by diffusion of hydrolyzed species through a residual layer, rather by surface reaction. This behavior is observed for any NaOH concentration; dissolution rate (k) is related to the first order of concentration (Fig. 6b). For a 5 mol L^{-1} solution concentration, SEM observations revealed nanowiskers growth on CDCp coating (Fig. 7), not detected by XRD analysis. They are supposed to be composed of sodium phosphate. These results, and the presumed disruption of thermogravimetric data by such compounds, argued further studies were restrained to the following washing protocol: 1 h at 80 °C with a 1 mol L^{-1} stirred solution. An apparent activation energy of 62 kJ mol^{-1} with this concentration inferred from the Arrhenius diagram (Fig. 6c). This value is close to 43 kJ mol^{-1} of T. Saeki et al. estimated for $Si_3(PO_4)_4$ dissolution in borax ($Na_2B_4O_7$) buffer [38]. It is noteworthy mentioning other dissolution tests were performed in ammonia solution as substitute to alkali hydroxide. Nevertheless, a passivation phenomenon by silica gel disturbed the reaction rate (not linear with time) and could not be fully eliminated in distilled water, arguing this path was discarded.

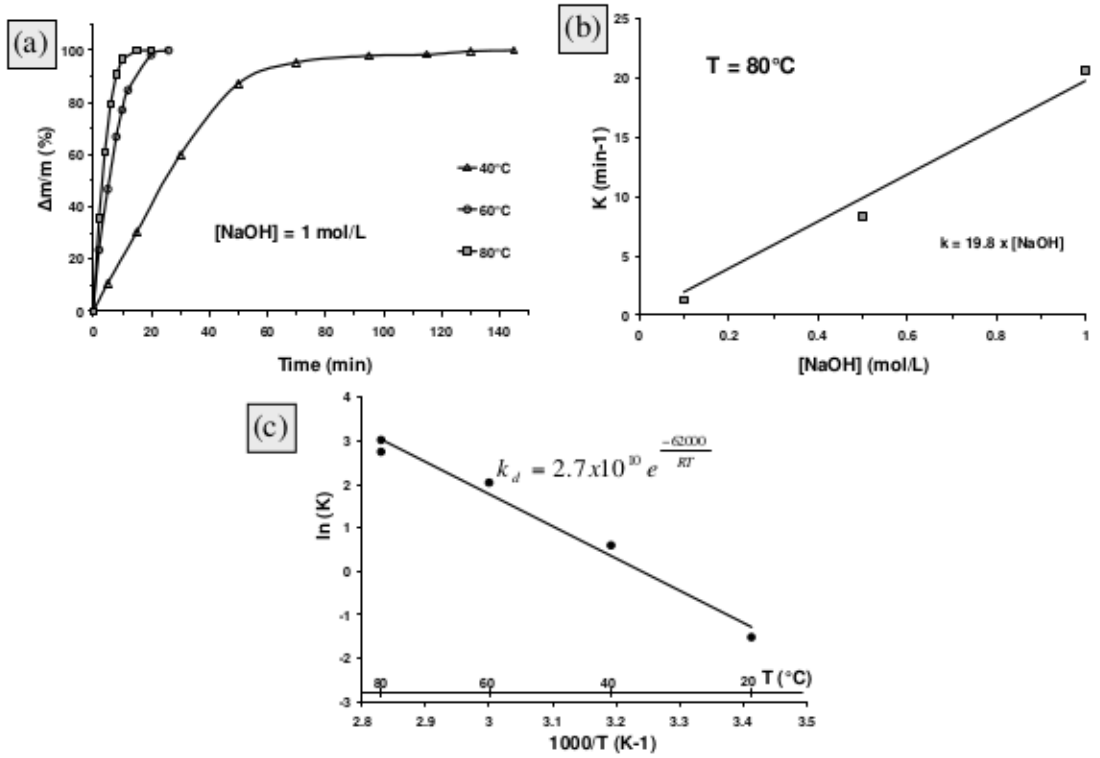

Fig. 6: Dissolution kinetics of SiP_2O_7 formed by SiC fiber phosphatation with CDCp-800 conditions: (a). effect of bath duration or temperature, (b). effect of bath concentration and (c). Arrhenius plots.

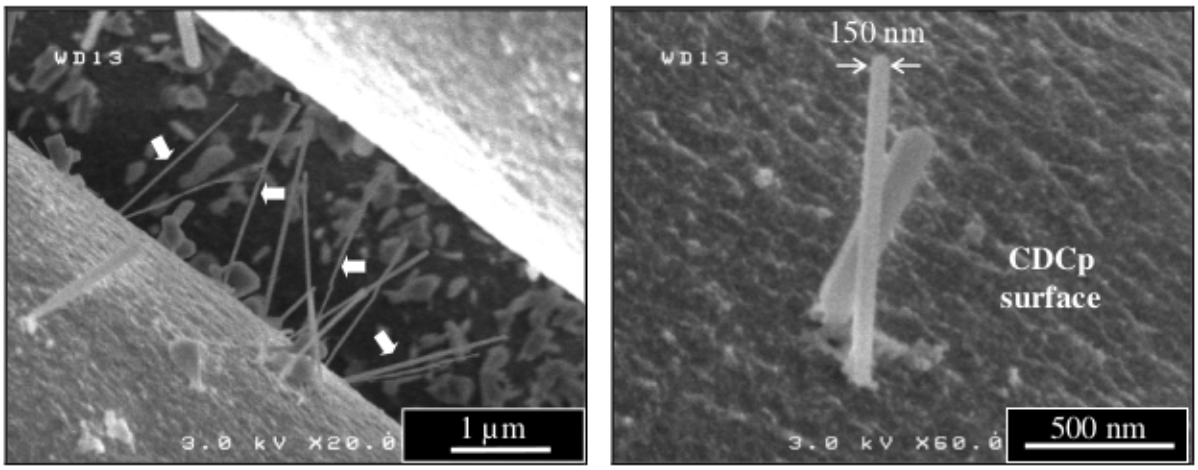

Fig. 7: SEM micrographs of nanowiskers (arrows) growth at the CDCp surface observed after high concentrated alkali hydroxide bath (5 mol L^{-1} NaOH).

Coating morphologies before and after washing step (Figs. 8–11) indicates the CDCp corresponded to so identified carbon rich layers for the different conditions (Table 2). CDCp-

700 and CDCp-800 dissolution resulted in a homogeneous and 1−2 µm thick CDCp coating as expected after Figs. 5c−d. As far as CDCp-600 surface is concerned, concentric tubes with thicknesses between 50 and 200 nm were observed (Fig. 9).

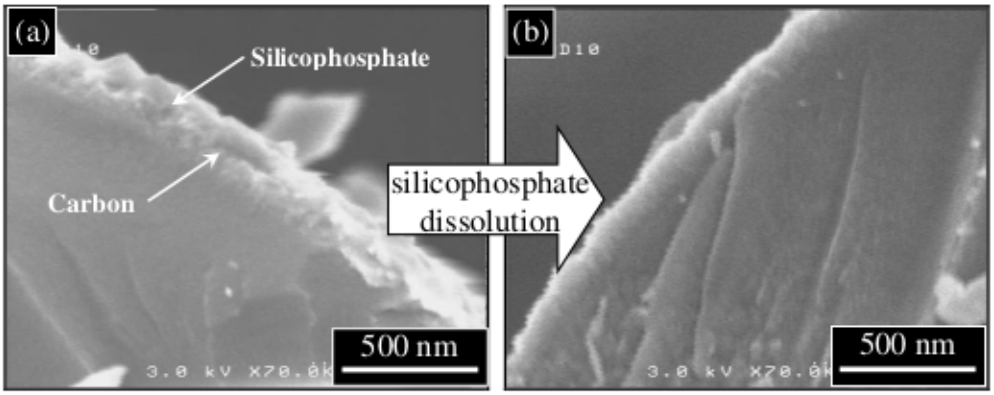

Fig. 8: SEM micrographs before (a). and after (b). alkali hydroxide bath of (1 mol L^{-1} NaOH at 80 °C) of CDCp-580 phosphated Grade-S SiCO fibers showing homogeneous CDCp coating.

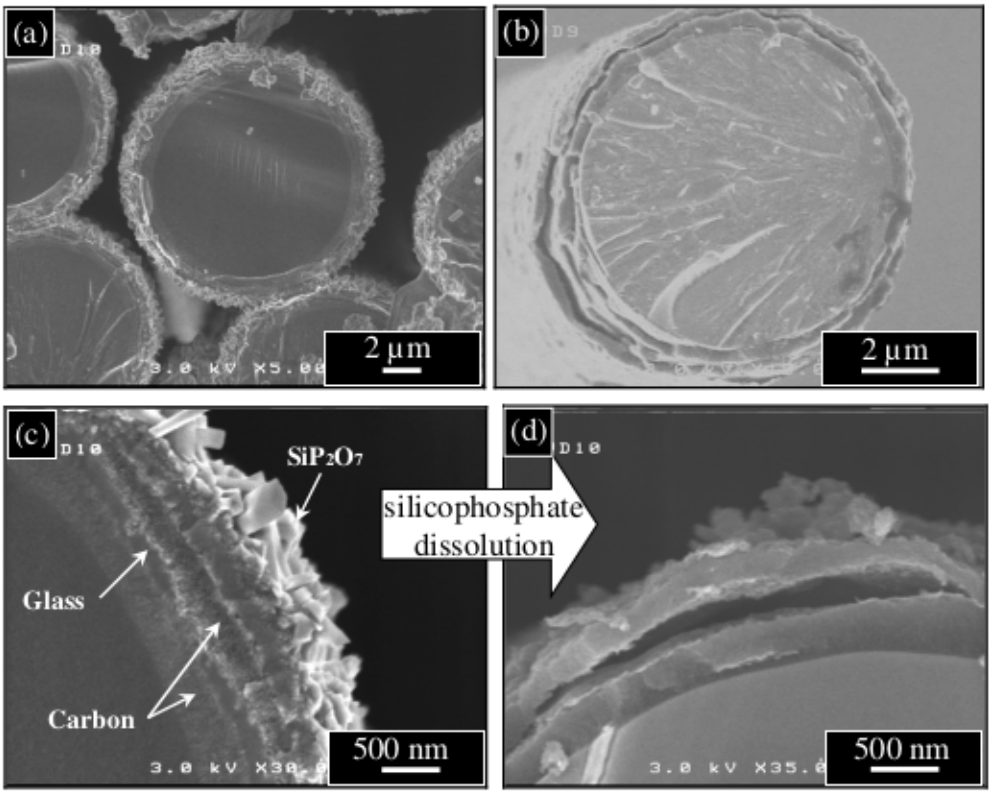

Fig. 9: SEM micrographs before (a,c). and after (b,d). alkali hydroxide bath of CDCp-600 samples presenting a tubular morphology of CDCp.

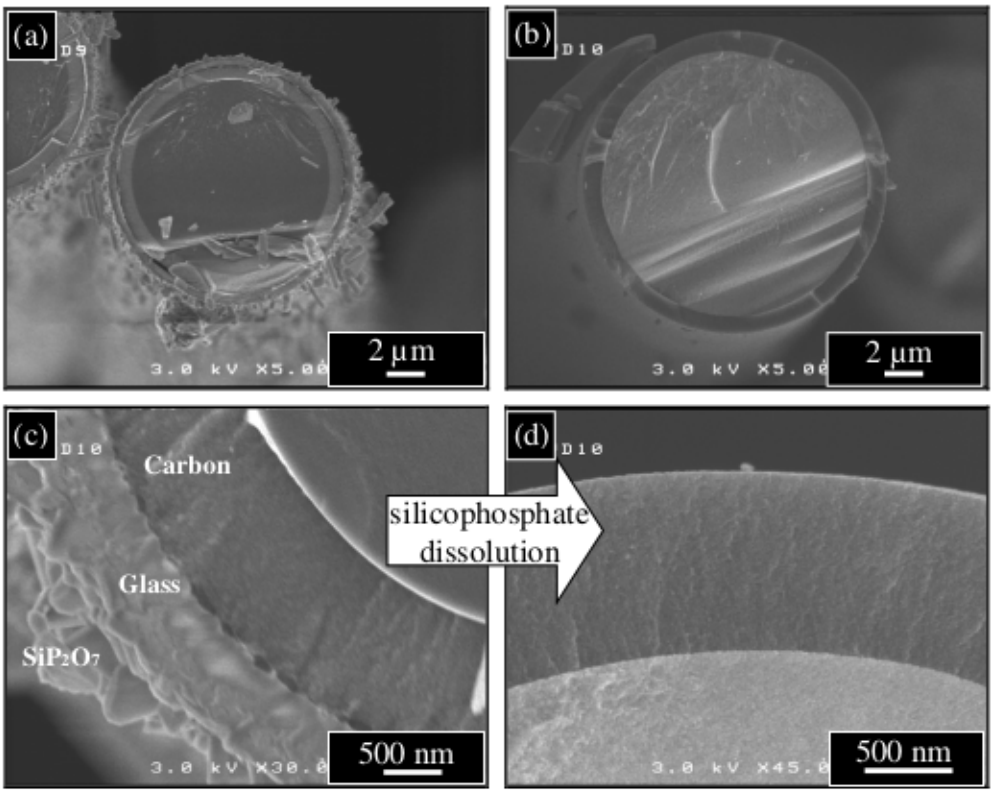

Fig. 10: SEM micrographs before (a,c). and after (b,d). NaOH bath of CDCp-700 samples presenting a single layer of CDCp.

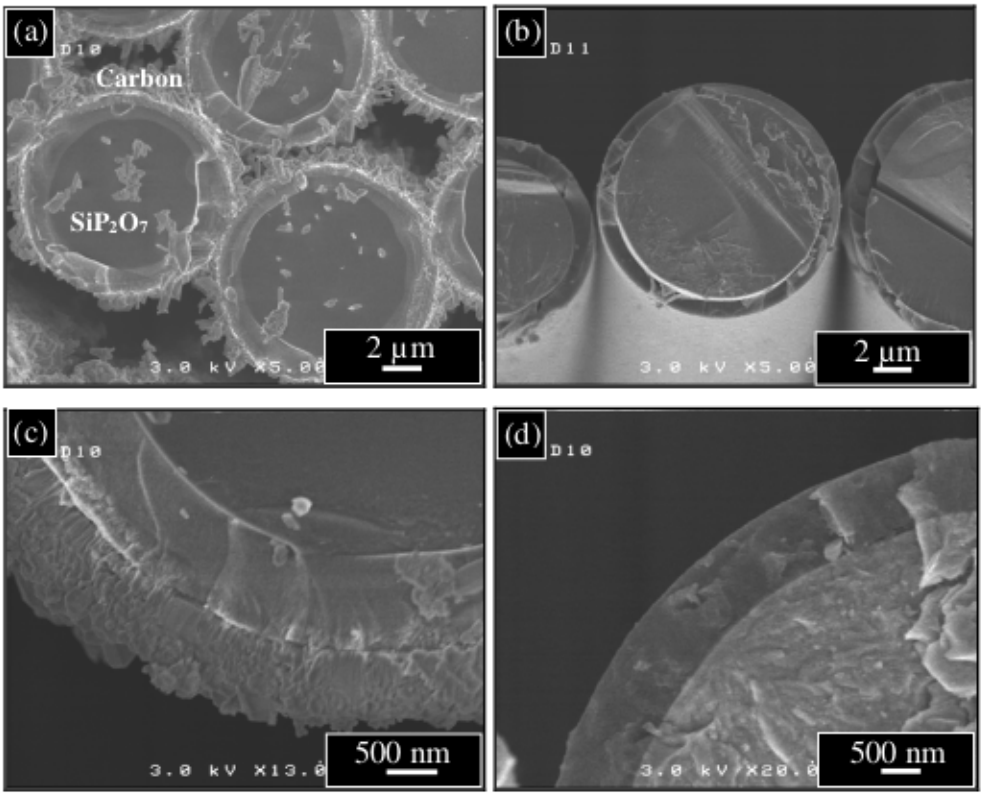

Fig. 11: SEM micrographs before (a,c). and after (b,d). alkali hydroxide bath of CDCp-800 samples presenting a single layer of CDCp.

3.2 Nitrogen physisorption experiments

Effect of phosphating treatment settings on PSD was studied by physisorption experiments, recorded at 77 K, on CDCp-600, CDCp-700, CDCp-800 and CDCp-tt (Grade-S substrate) after washing treatment. The porosity detected was ascribed to the only CDCp coating, as no porosity could be highlighted on as-received Grade-S fibers (SSA = 1.04 $m^2 g^{-1}$). Two distinct sample masses were considered to analyze N_2 physisorption results as discussed in method section: (i). whole sample mass (CDCp + untransformed core) or (ii). estimated CDCp mass, considering its weight fraction assessed by TGA measurement. Carbon derived from phosphating treatments followed by alkali hydroxide washing shows a large adsorbed nitrogen volume for low partial pressure and a H2 type hysteresis loop [53], between adsorption and desorption branches (Fig. 12a,b). Therefore, and according to IUPAC

classification, CDCp is a type I and IV material displaying micropores (pore width < 2 nm) and mesopores (Fig. 12c,d, pore size between 2 and 50 nm) [56]. As nitrogen is adsorbed over the whole range of microporosity partial pressure (P/P_0 < 0.4) (Fig. 12a), a broad micro-PSD can be suggested. Moreover, CDCp-600 sample highlights macroporosity (pore diameter >50 nm), revealed by adsorbed volume enhancement at P/P_0 > 0.9, which could be ascribed to the space separating CDCp tubes.

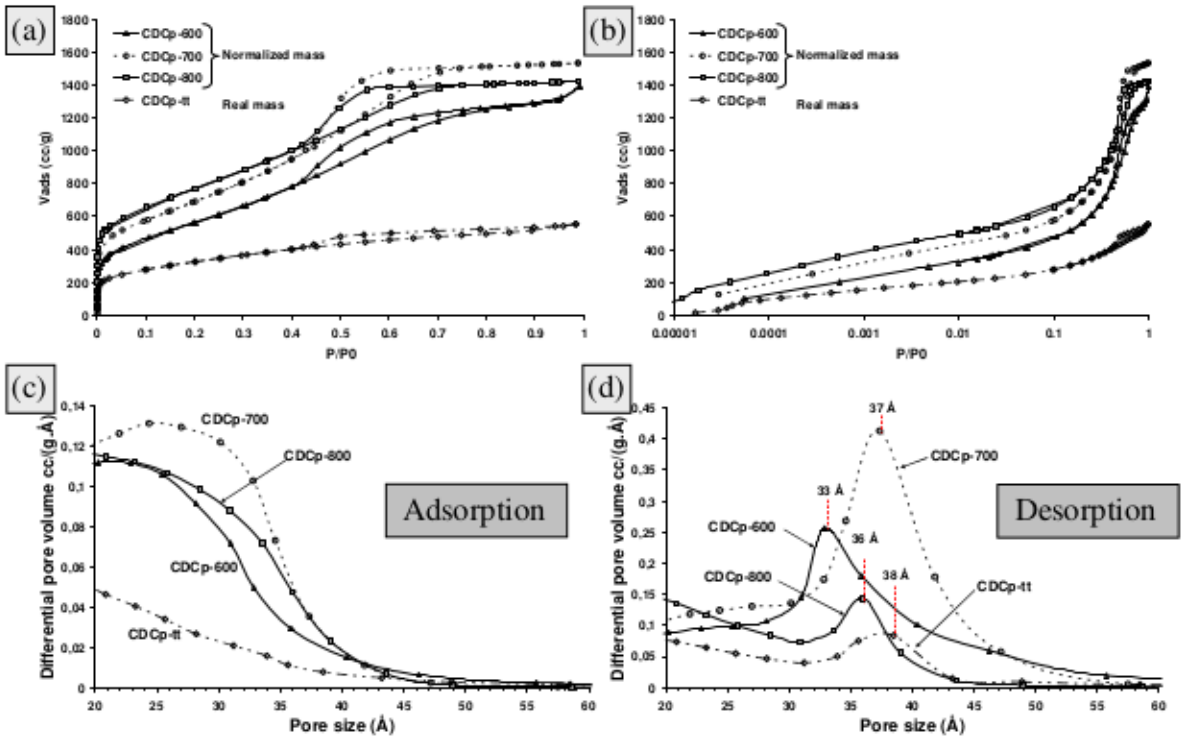

Fig. 12: Grade-S derived carbon, resulting from phosphating–NaOH cleaning etching process, porosity microstructure characterization: (a,b). nitrogen adsorption-desorption isotherms, (c). mesopore size distribution using BJH method on adsorption branch or (d). desorption branch. CDCp-600, CDCp-700 and CDCp-800 data were corrected estimating the carbon coating mass after TGA experiments.

Table 3 summarizes pore structure properties of these samples, calculated with their uncorrected mass (CDCp + untransformed core). For comparison purpose, the Grade-S-DC,

resulting from pure chlorine etching treatment for 2 h at 575 °C, can be found in Table 4. Equivalent specific surface area (SSA) of samples CDCp-600, CDCp-700 and CDCp-800 strongly depends on the carbon layer thickness when the considered mass is not corrected. Totally transformed fibers overcome this problem and show an equivalent specific surface area of 1120 $m^2 g^{-1}$ associated with effective micropore volume of 0.50 $cm^3 g^{-1}$. Post-correction of the sample mass gives equivalent specific surface area of 2020 $m^2 g^{-1}$, 2470 $m^2 g^{-1}$ and 2690 $m^2 g^{-1}$ and total pore volume ($V_{p,0.99}$) above 2 $cm^3 g^{-1}$, respectively for CDCp-600, CDCp-700 and CDCp-800. Such high specific surface area, usually measured on activated carbon [7,18,42], is found to increase with the treatment temperature. Albeit arising from an identical treatment temperature, CDCp-tt and CDCp-700 (corrected mass) highlight SSA and pore volume discrepancies (Table 3, Fig. 12) questioning the sample mass estimation approach. This may, nonetheless, infer from extended treatment duration for CDCp-tt production (Table 2) and potential over-activation or collapsed porosity (compressive strained by expanding glass devitrification (Fig. 5 f-h)), where CDCp-700 is likely unstrained and in default of phosphorus as indicated by non-devitrified glass phase (Figs. 5c and 10).

Sample	SSA ($m^2 g^{-1}$)	Vol µp ($cm^3 g^{-1}$)	µpores size (Å)	C param. a.u.	Vol meso ($cm^3 g^{-1}$)	$V_{p,0.99}$ ($cm^3 g^{-1}$)
CDCp-600	100	0.043	8.9	170	0.055	0.10*
CDCp-700	390	0.17	8.1	240	0.18	0.38
CDCp-800	270	0.12	7.6	660	0.078	0.22
CDCp-tt	1120	0.50	7.9	825	0.25	0.80

Table 3: Data extracted from N_2 sorption at 77 K using BET equation, H-K and BJH (adsorption branch, pore > 40 Å) methods, using non-corrected sample mass. (*) the total pore volume of CDCp-600 was assessed with the adsorbed volume at 0.90 P/P_0 due to macroporosity.

Sample	Etching T° (°C)	SSA ($m^2 g^{-1}$)	Vol µp ($cm^3 g^{-1}$)	µpores size (Å)	C param. a.u.	Vol meso ($cm^3 g^{-1}$)	$V_{p,0.99}$ ($cm^3 g^{-1}$)
NL207-DC	675	1670	0.75	8.2	600	0.025	0.89
Grade-S-DC	575	860	0.37	6.4	5000	0.011	0.43
Lox-M-DC	650	1240	0.55	8.2	500	0.021	0.68
ZMI-DC	700	1500	0.67	8.1	480	0.020	0.77
Hi-Ni-DC	850	1180	0.48	6.1	37000	0.001	0.49*

Table 4: Comparison of SiC-based fiber derived carbon pore structure after chlorination etching treatment of 2 h, assessed by nitrogen physisorption at 77 K (H-K and BJH methods). (*) the total pore volume was assessed for a partial pressure of 0.90 P/P_0 due to macroporosity.

Carbon derived from other SiC-based fibers are also micro-mesoporous (Fig. 13a) with equivalent specific surface area exceeding 1000 $m^2 g^{-1}$ (corrected sample mass) and total pore volume larger than 0.7 $cm^3 g^{-1}$ (Table 5). Hi-Ni-DCp displays macroporosity as well, which could be attributed to the large silicophosphate domains (granular morphology) found after phosphate etching [36]. Apparent inconsistency of median micropore size, between 7 and 9 Å for CDCp issued from Grade-S (Table 3), Lox-M, Hi-Nicalon and about 11 Å for NL207-DCp and ZMI-DCp, should not be interpreted as the latter is directly related to the lack of data for low partial pressure (limited to 0.016 against 0.003 P/P_0 Fig. 13a). Micropore size for CDCp higher than 7.5 Å but below 9 Å for all sample could be assumed, value similar or above the CDC-PSD ones (Table 4). Meso-PSD of CDC or CDCp carbons highlight an artificial shoulder or peak between 30 and 40 Å (Figs. 12d, 13c,d) when extracted from desorption branch, not identified on the adsorption-derived branch (Fig. 12c). This phenomenon is related to sudden condensate evaporation due to cavitation phenomenon, further developed in discussion section. The total pore volume ($V_{p,0.99}$) is coherent with the values of micro plus mesoporosity, derived from H-K and BJH methods. For CDC materials, the ratio of micro to mesopore volume lies about 30 whereas it ranges between 0.8 and 6 on CDCp, with a tendency to increase with the phosphating treatment temperature (Table 3).

Carbon derived from a phosphatation process hence displays more mesoporosity (Figs. 13c,d), likely associated with the mechanism of their formation (cf. discussion section).

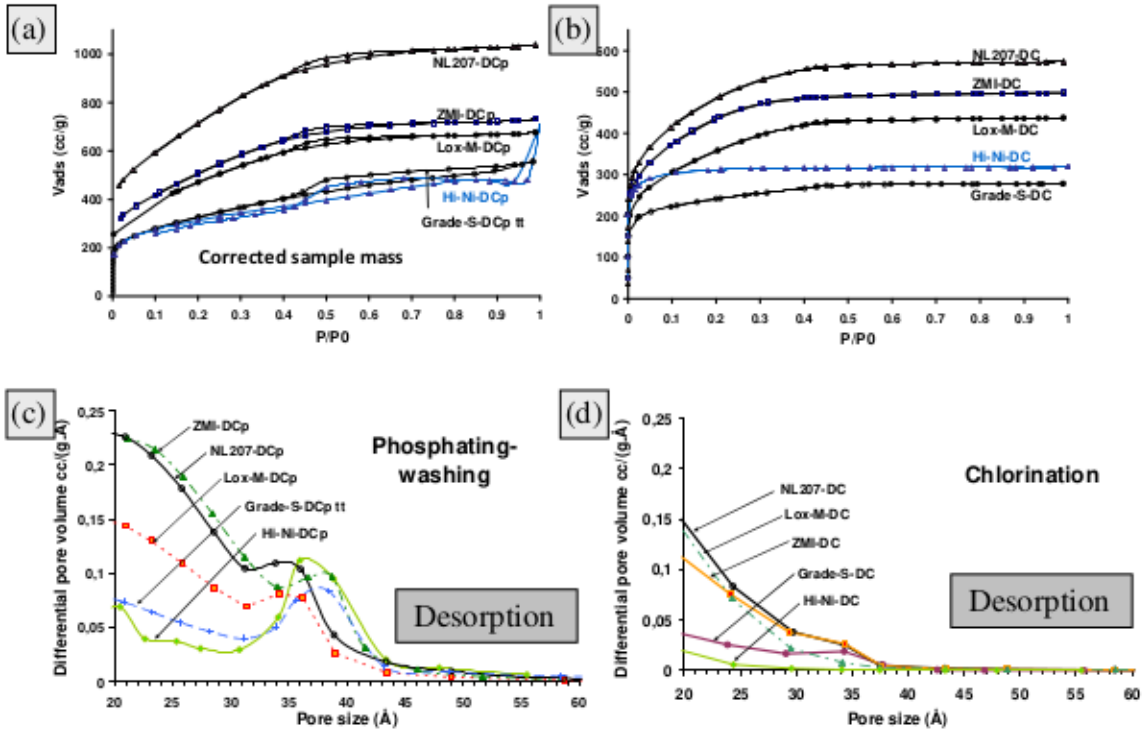

Fig. 13: Nitrogen physisorption isotherms and associated BJH-derived PSD (calculated from desorption branch) on carbon derived from NL207, Hi-Nicalon, Grade-S, Lox-M and ZMI by (a,c). phosphating/washing considering the corrected sample mass or (b,d). chlorination etching treatment on fully transformed samples.

Sample	SSA ($m^2\ g^{-1}$)	Vol µp ($cm^3\ g^{-1}$)	µpores size (Å)	C param. a.u.	Vol meso ($cm^3\ g^{-1}$)	$V_{p,0.99}$ ($cm^3\ g^{-1}$)
NL207-DCp	2550	1.10	11.0	135	0.20	1.6
Lox-M-DCp	1650	0.73	8.6	330	0.12	1.0
ZMI-DCp	1810	0.78	11.3	120	0.13	1.3
Hi-Ni-DCp	1070	0.48	8.8	840	0.20	0.73

Table 5: Comparison of SiC-based fiber derived carbon pore structure after phosphating etching treatment (Table 2) assessed by nitrogen physisorption at 77 K (H-K and BJH methods). CDCp properties are calculated using the corrected sample mass after TGA analysis under pure dry oxygen.

3.3 Oxidation behavior of CDCp

Fig. 14 presents thermogravimetric analysis (TGA) of Grade-S-DC or Grade-S-DCp, respectively stemming from chlorination and phosphating etching treatments. The mass loss starting temperature (300 °C) or the rate does not seem drastically impacted by etching process. Grade-S-DC samples had been demonstrated to be more sensitive to oxidation than other SiC fibers-DC [31]. CDCp-700 and CDCp-800 display a slightly higher burn-off rate that could be ascribed to oxygen access, consequence of the larger pore volume (Table 3). Apparent activation energies of the oxidation (Table 6) were calculated considering an Arrhenius-like evolution of the kinetic constants with the temperature, inferred from first derivation of the curves in 300–500 °C range. These energies range between 66 and 87 kJ mol^{-1}, values below the Grade-S-DC one (98 kJ mol^{-1}) and other SiC-fibers-DC [25,31] or activated carbon [57]. Sodium contamination and its influence as oxidation catalyst might be pointed out, despite the washing process. As the phosphating temperature increases, the apparent activation energy raises, behavior likely related to carbon activation or organization with temperature.

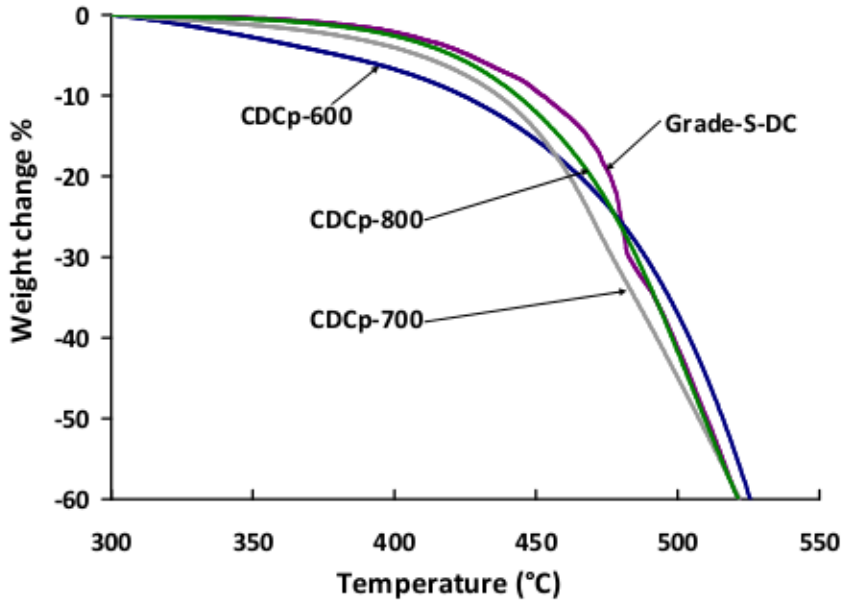

Fig. 14: TGA data for Grade-S fiber derived carbon, CDC or CDCp respectively resulting from chlorination or phosphating etching treatment, heated at 5 °C min^{-1} under pure and dry oxygen. Weight change was normalized to the carbon coating mass (10–20 mg).

Sample	Ea (kJ mol^{-1})	k_0 (s^{-1})
CDCp-600	66	3.0
CDCp-700	83	130
CDCp-800	87	260
Grade-S-DC	98	16

Table 6: Apparent activation energies defined by burn-off experiments in 300–500 °C range under pure and dry oxygen of Grade-S fiber derived-carbon via phosphating (CDCp) or chlorination (CDC) etching.

3.4 Mechanical properties

Direct measurement of CDCp mechanical properties by tensile test of fully transformed fibers, as reported after chlorination etching [31], was not feasible as samples lose their fibrous shape. Tensile tests were hence performed on CDCp-580, CDCp-600 and CDCp-800 partially transformed probes, to illustrate a possible benefit of here proposed etching treatment on fiber properties. This investigation was motivated by similar works on chlorinated SiC-

based fibers, highlighting a significant tensile strength increase when the firsts hundreds of nanometers where transformed, considering the only untransformed core section [24,26,32]. On Grade-S (8.5 µm diameter), this asymptotic strength improvement reached 20% with a 300 nm etching depth, about 3900 MPa. This was attributed to surface-located flaws depletion, revealed by fractographic analysis. This evolution was nevertheless not observed after phosphating etching (Table 7): tensile strength of CDCp-580 and CDCp-600 lies below the as-received fibers one, whereas CDCp-800 is equivalent, with similar statistical parameters. Young modulus stability confirms microstructure or composition of fiber core is not altered by this treatment. Critical flaw position and type were therefore identified by fractographic analysis to argue the absence of strength improvement or even its drop.

Fiber	σ_r (MPa) ± std dev	E (GPa)	ε_r (%)	m	σ_0 (MPa)
As-received	3200 ± 500	180	1.8	5.9	3400
CDCp-580	2500 ± 450	190	1.4	6.3	2700
CDCp-600	2750 ± 500	180	1.5	6.1	3000
CDCp-800	3300 ± 800	190	1.5	4.5	3600

Table 7: Mechanical properties assessed by tensile testing of as-received or etched Grade-S SiC-based fibers, considering the untransformed core diameter.

The fracture surfaces of transformed fibers show the classical pattern for brittle materials with mirror, mist, hackle and branching regions concentric to the flaw [58]. This allowed the critical flaw location and classification in five different types as follow (Figs. 15−17):

- i-a internal-located defect;
- s-a surface-located defect but no trace;
- s-e surface-located structural heterogeneity;
- is-a internal defect situated at transformation front thus converted to surface-located defect;
- h-a inhomogeneous etching depth.

The proportion of surface-located flaws is rather stable and close to 100% before (s-a, s-e) and after (s-a, s-e, is-a, h-a) phosphating etching. Defect types i-a, s-a and s-e are classically reported on as-received fibers [59,60] whereas is-a were observed after chlorination and typical for surface etched fibers. This latter defect type represents about 10% of fiber defect whatever the treatment condition. The transformation heterogeneity (h-a) (Figs. 15b and 16c-d) was not reported after chlorination etching and reveals the difficulty to control the phosphating transformation rate or possible phenomenon at fiber contact location (Fig. 11a). This defect type is observed with a frequency of respectively 5%, 10% and 0% on CDCp-580, CDCp-600 and CDCp-800, based on sampled fiber sets. It is likely caused by fast elemental phosphorus diffusion at lower temperatures, where the oxygen content in the system, coming from oxidizing water vapor, is low. Defect h-a led to drastic individual strength drop when observed. However, only few of the individual strengths measured on CDCp-580 and CDCp-600 exceeded the mean value, 3200 MPa, of as-received fibers. Therefore, h-a defect type can not by itself explain this strength decrease. Another source of embrittlement should exist but was not identified in this work.

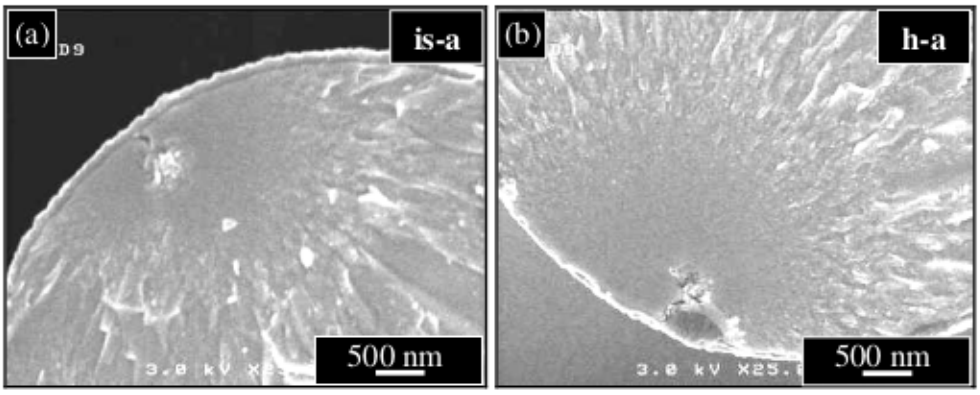

Fig. 15: SEM analysis of CDCp-580 treated and washed fiber fracture surface: (a). former internal defect located at reaction front (is-a) and (b). transformation heterogeneity h-a.

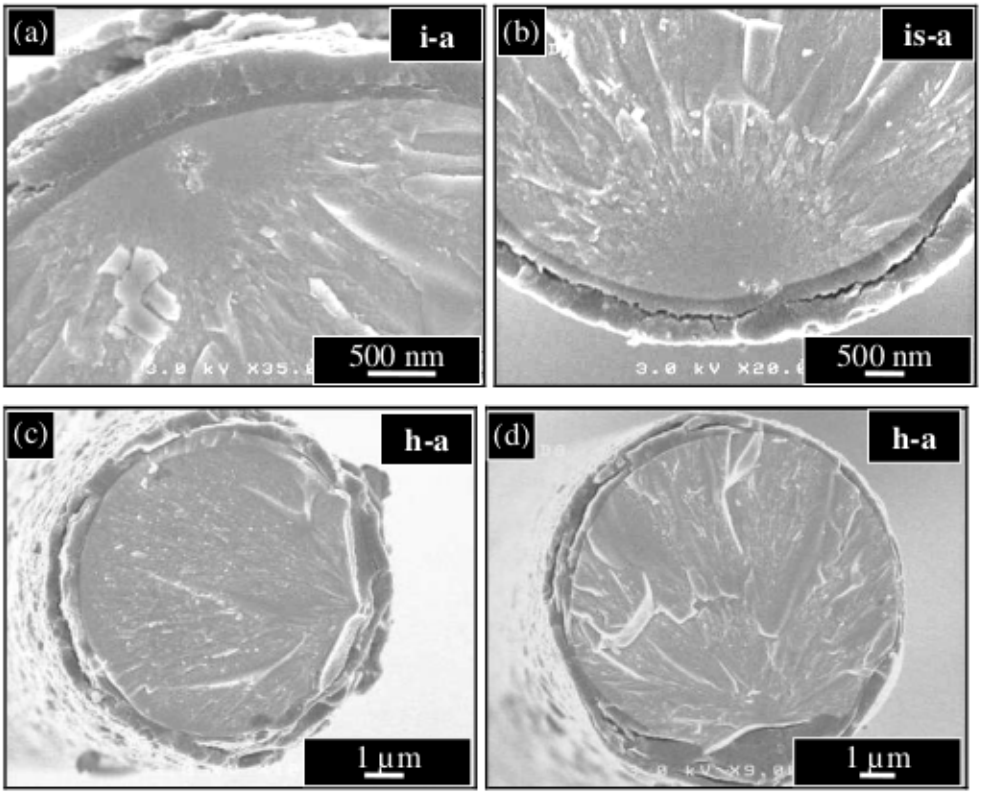

Fig. 16: SEM micrographs of CDCp-600 treated fiber fracture surface: (a). internal defect (i-a), (b). former internal defect situated at transformation front thus transformed into surface-located flaw (is-a) or (c–d). transformation heterogeneity (h-a).

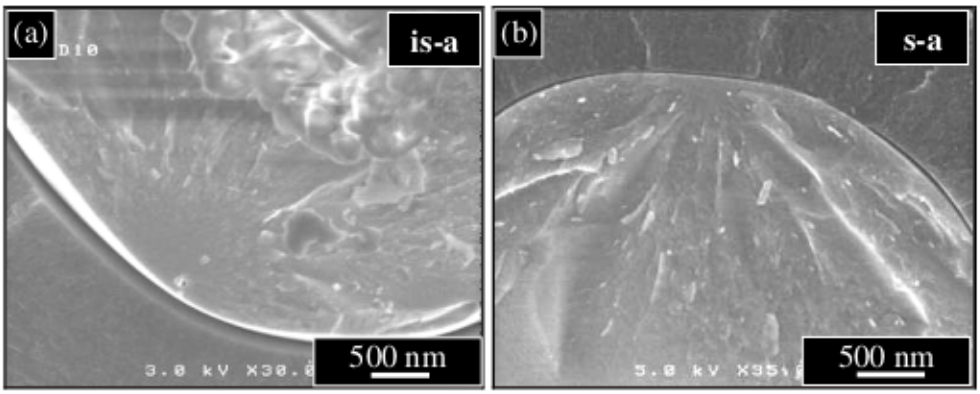

Fig. 17: SEM analysis of CDCp-800 treated fiber fracture surface: (a). is-a defect or (b). no trace (s-a).

4 Discussion

CDC, derived from halogenation, and CDCp, derived from phosphatation, are both micro and mesoporous materials in different extend, obtained etching silicon atoms from non porous SiC-based fibers. Both, treatment temperature and substrate type (microstructure or chemical composition) can be used to tune their PSD. The influence of phosphating condition on CDCp microstructure is underlined by median micropore size which decreases when the etching temperature increases (Table 3). Nonetheless, this median micropore size remains above the 6.4 Å of CDC (Table 4) measured for the same Grade-S precursor. The same apply to others fiber types (Table 5). It is worth noting Grade-S-DC displays atypical properties compared to carbon derived from other SiC-based fibers [31], phenomenon attributed to low chlorination temperature used for its synthesis (<600 °C). A similar evolution with etching temperature was observed after chlorination etching of ZrC, TiC, Al_4C_3 in 400−1400 °C range [13,23] whereas an opposite behavior has been reported on Ti_3SiC_2 in the 300−700 °C range [61].

On Grade-S-DCp, two distinct hysteresis loops were observed: (i). progressive condensate evaporation in the $0.4 < P/P_0 < 0.9$ partial pressure range for CDCp-600 or (ii). steeped loop closing about 0.45 P/P_0 for CDCp-700, CDCp-800 and CDCp-tt (Figs. 14a,b). Former hysteresis loop is likely associated with capillary condensation that takes place in opened and necked mesopores. The partial pressure for which latter loop is closed indicates a cavitation controlled evaporation of the capillary condensate from mesopores, that are obstructed by the pore constriction (ink bottle-like with neck size < 4 nm), and related to the nature of the adsorptive or temperature [52,53,56]. Consequently, the desorption-derived PSD is expected to highlight artificial pores, deduced from the sudden capillary condensate evaporation of larger mesopores [56,62]. Indeed, discrepancy between adsorption (Fig. 14c) and desorption (Fig. 14d) derived meso-PSD was evidenced in result section by a narrow artificial peak

between 33 and 38 Å on the latter. However, mesopores with sizes ranging from 20 to 45 Å, observed on adsorption and desorption-derived BJH PSD, albeit not well described by this method, would be representative of capillary condensate evaporation not driven by pore blocking. It should be noted the adsorption branch is not in thermodynamic equilibrium and shall therefore be limited in exploitation.

The same hysteresis behavior was observed on carbon derived from other SiC-based fibers by phosphating etching (Fig. 13c) or chlorination (Fig. 13d). This could, in this latter case, be related to the substrate oxygen content (first-generation fibers) and consequent partial oxidation during the etching process [22]. The broad micropore size distribution, suggested by extended partial pressure range where nitrogen is adsorbed (Fig. 13b), would likely indicate such partial oxidation. Hi-Ni-CD and ZMI-DC substrates did not highlight such mesoporosity (Fig. 13d), however observed on corresponding CDCp (Fig. 13c), which indicates another source of pore enlargement is then active.

This statement is in agreement with C parameter values, extracted from BET equation. Indeed, that parameter, independent to sample mass or volume, is an indicator of adsorbant-adsorbate interaction and associated with adsorption on high-energy surface sites when exceeding 150 [53]. It overpassed this value for most of CDCp, excepting NL207-DCp and ZMI-DCp (Table 5), and found to increase, on Grade-S substrate, with the phosphating-activation severity or temperature (Table 3). If noticeable, these values stand much below values calculated on CDC, regardless the precursor type (Table 4), revealing surface chemistry differences between these etching routes. The highest recorded values for CDCp stand at 825 or 840 respectively for CDCp-tt and Hi-Ni-DCp. These materials seem to show a complete silicophosphate devitrification (Fig. 5f-h) [36] which argue a stronger chemical

activation by H_3PO_4 in excess. Progressive increase with treatment temperature of C parameter, equivalent SSA and micropore-mesopore volume ratio (Table 3) confirms this hypothesis. On CDC, similar activation post treatments were reported by KOH [17], air or CO_2 [18–20,63] showing the same tendency.

If oxidation activation can result in pore enlargement generating mesoporosity, another possible origin might here be pointed out for phosphate etching process: the initial stage of demixing between carbon and silicophosphate glass. Indeed, carbon layer contains a non-negligible amount of silicophosphate glass (Fig. 18) that would likely be found as nanoscale demixed domains surrounded by carbon phase, generating mesoporosity after NaOH dissolution as identified by nitrogen physisorption. A hierarchical pore structure of CDCp material might exist, induced by progressive demixion/coalescence mechanism related to glass domains composition: from 10 mol.% P_2O_5 near the interface with untransformed fiber core to 20 mol.% P_2O_5 on the last µm (Fig. 18). This could however not be evidenced in this work by SEM nor high resolution TEM micrographs. An extreme case of such hierarchy is the layered morphology (Fig. 5g,h), resulting in concentric tubular CDCp morphology which retains a particular interest. It was observed on all first-generation fibers in the 600–700 °C range with large number of glass layers (Fig. 19). Another morphology consisting in lenticular glass domains surrounded by carbon layer (Fig. 20) can also be observed with similar conditions.

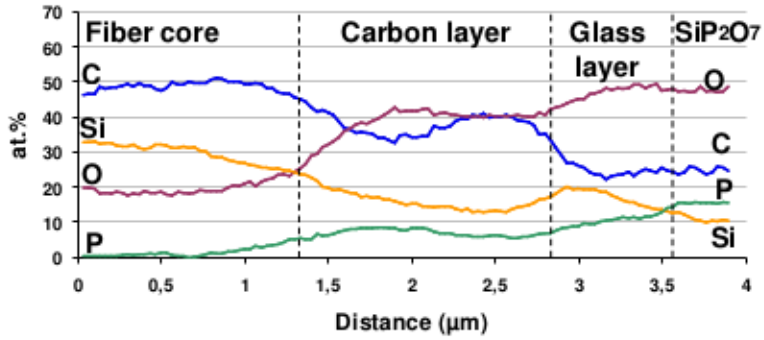

Fig. 18: Energy dispersive X-ray spectroscopy profile of Grade-S fiber section phosphated in CDCp-700 conditions (Table 2 and Fig. 10), performed on ion milled TEM sample (30 kV acceleration tension). The silicophosphate contamination in outer carbon layer shows the same composition (20 mol.% P_2O_5) than the glass layer.

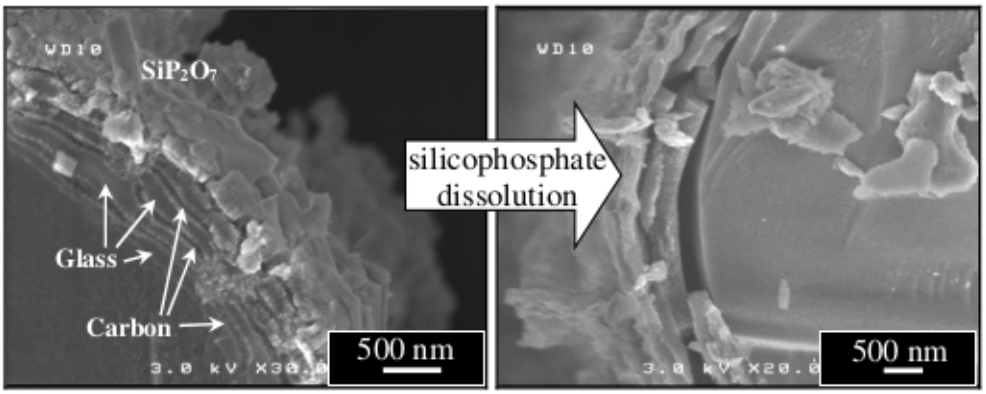

Fig. 19: Tubular CDCp morphology obtained on NL207 fabric after a 4h treatment at 600 °C (7.3×10^{-2} mL min^{-1} acid and 450 NmL min^{-1} N_2 flows).

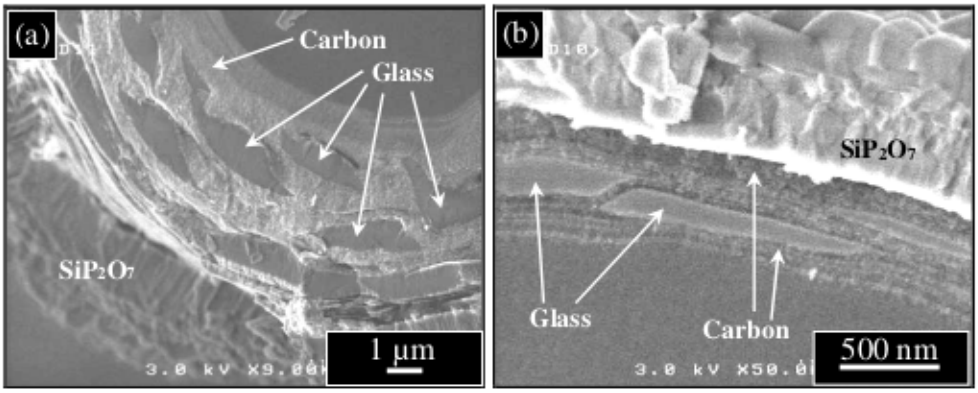

Fig. 20: Lenticular morphology (glass domains surrounded by carbon rich phase) obtained on a NL207 tow after following phosphating treatment: (a). 650 °C for 4 h (7.3 x 10^{-2} mL min^{-1} acid and 83 NmL min^{-1} N_2 flows) and (b). 700 °C for 1 h (1.4 x 10^{-1} mL min^{-1} acid and 250 NmL min^{-1} N_2 flows).

Because phosphating etching kinetic is linear with time, this route offers the possibility to form CDCp with controlled thicknesses on complex geometries. As long as silicophosphate phase is not devitrified (partially transformed fibers), so obtained carbide derived carbon display very high equivalent SSA with unique and spontaneous interesting morphologies. Moreover, untransformed fiber core provides some handability and mechanical properties, required for specific applications.

5. Conclusions

A new route to produce carbide-derived carbon by a two-steps process from SiC-based fibers could be achieved by (i). transforming silicon atoms in a silicate phase, in which carbon solubility is limited, (ii) afterward chemically eliminated. Homogeneous transformation thicknesses could be obtained on complex geometries and evolved linearly with etching time. This coating is micro-mesoporous (equivalent SSA > 1000 m^2 g^{-1}, pore volume > 0.7 g cm^{-3}) with a tunable pore size distribution adjusting treatment conditions or substrate chemistry-microstructure. Coatings with estimated specific surface area exceeding 2000 m^2 g^{-1} were

obtained on partially transformed first-generation fibers. Compared to chlorination derived carbon, CDCp highlighted a higher volume of mesoporosity which could be ascribed to (i). pore enlargement resulting from oxidation chemical activation (oxygen content of as-received fiber or reactive species), or (ii). recombination of carbon atoms around glass domains. Chemical stability of CDCp against oxidant species appeared low as burn-off started at 300 °C. Phosphating etching, contrary to chlorination, did not highlighted tensile strength improvement of the untransformed fiber core. Fractographic analysis revealed some transformation heterogeneities, not observed after chlorination treatment, partially explaining this difference.

The high equivalent SSA obtained and mechanical properties brought by fiber core, are novelties this original carbide etching route offers. Possible applications are currently being reviewed in CDC development. Adsorbents, gas storage, catalyst or electrochemical applications are some examples. Mesoporosity may also improve impregnation processes to form new interphases materials on individual fibers by a different route than extensively used chemical vapor infiltration. It is worthy to note that the attractive multilayer or lenticular transformation morphologies, leading to CDCp tubes or pockets with additional shaped macroporosity, open other potential applications. Mastering the silicate phase chemistry-crystallography and their demixion-coalescence depicts new insight into CDC-PSD fine tuning.

Acknowledgment

The authors acknowledge the financial support of the Snecma Propulsion Solide, now Safran ceramics, for this work. This research did not receive any specific grant from funding agencies in the public, commercial or not-for-profit sectors.

References

[1] K. Okamura, Ceramic fibres from polymer precursors, Composites 2 (1987) 107–120.
doi: 10.1016/0010-4361(87)90489-7

[2] R. Naslain, The design of the fibre-matrix interfacial zone in ceramic matrix composites, Composites Part A 29A (1998) 1145–1155.
doi: 10.1016/S1359-835X(97)00128-0

[3] J.W. Faust, Silicon carbide A High Temperature Semiconductor. New York: O'Connor Smiltens; (1960) 403–419.

[4] D. Zhuang, J.H. Edgar, Wet etching of GaN, AlN and SiC: a review, Mat. Sci. Eng. R48 (2005) 1–46.
doi: 10.1016/j.mser.2004.11.002

[5] Y. Gogotsi, I.D. Jeon, M.J. McNallan, Carbon coatings on silicon carbide by reaction with chlorine-containing gases, J. Mat. Chem. 7 (1997) 1841–1848.
doi: 10.1039/a701126a

[6] N. Batisse, K. Guerin, M. Dubois, A. Hamwi, The synthesis of microporous carbon by the fluorination of titanium carbide, Carbon 49 [9] (2011) 2998–3009.
doi: 10.1016/j.carbon.2011.03.018

[7] M. Wunder, B. Jeanneret, Sur l'action de l'acide phosphorique sirupeux sur divers alliages obtenus au four électrique, Aca. Sci. Paris 152 (1911) 1770–1771.

[8] M. Kusunoki, M. Rokkaku, S. Suzuki, Epitaxial carbon nanotube film self-organized by sublimation decomposition of silicon carbide, Appl. Phys. Lett. 71 [18] (1997) 2620–2622.
doi: 10.1063/1.120158

[9] Z.G. Cambaz, G.N. Yushin, Y. Gogotsi, Formation of carbide-derived carbon on β-silicon carbide whiskers, J. Am. Ceram. Soc. 89 [2] (2006) 509–514.
doi: 10.1111/j.1551-2916.2005.00780.x

[10] Y. Gogotsi, S. Welz, J. Daghfal, M.J. McNallan, I.D. Jeon, K.G. Nickel, Formation of carbon coating on SiC fibers by selective etching in halogens and supercritical water, Ceram. Eng. Sci. Proc. 19 [3] (1998) 87–94.
doi: 10.1002/9780470294482.ch10

[11] Y. Gogotsi, M. Yoshimura, Formation of carbon films on carbide under hydrothermal conditions, Nature 367 (1994) 628–630.
doi: 10.1038/367628a0

[12] N.S. Jacobson, Y. Gogotsi, M. Yoshimura, Thermodynamic and experimental study of carbon formation on carbides under hydrothermal conditions, J. Mater. Chem. 5 [4] (1995) 595–601.
doi: 10.1039/jm9950500595

[13] G. Yushin, A. Nikitin, Y. Gogotsi, Carbide-derived carbon. In: Gogotsi Y, editor. Nanomaterials Handbook, CRC Taylor&Francis (2006) 239–82.
doi: 10.1002/anie.200685445

[14] A. Lee, R. Zhu, M.J. McNallan, Kinetics of conversion of silicon carbide to carbide derived carbon, J. Phys. Cond. Mater. 18 (2006) 1763–1770.
doi: 10.1088/0953-8984/18/32/S07

[15] Y. Gogotsi, R.K. Dash, G. Yushin, T. Yildirim, G. Laudisio, J.E. Fischer, Tailoring of Nanoscale Porosity in Carbide-Derived Carbons for Hydrogen Storage, J. Am. Chem. Soc. 127 [46] (2005) 16006–16007.
doi: 10.1021/ja0550529

[16] M. Kormann, H. Gehard, N. Popovska, Comparative study of carbide-derived carbons obtained from biomorphic TiC and SiC structures, Carbon 47 (2009) 242–250.
doi: 10.1016/j.carbon.2008.10.002

[17] C. Portet, M.A. Lillo-Rodenas, A. Linares-Solano, Y. Gogotsi, Capacitance of KOH activated carbide-derived carbons, Phys. Chem. Chem. Phys. 11 (2009) 4943–5.
doi: 10.1039/B816514A

[18] S.H. Yeon· S. Osswald, Y. Gogotsi, J. P. Singer, J. M. Simmons, J. E. Fischer, M. A.Lillo-Ródenas, Á. Linares-Solano, Enhanced methane storage of chemically and

physically activated carbide-derived carbon, J. Power Sources 191 (2009) 560–567.
doi: 10.1016/j.jpowsour.2009.02.019

[19] M. Kormann, N. Popovska, Processing of carbide-derived carbons with enhanced porosity by activation with carbon dioxide, Microp. Mesop. Mater. 130 (2010) 167–173.
doi: 10.1016/j.micromeso.2009.10.028

[20] M. Schmirler, F. Glenk, B.J.M. Etzold, In-situ thermal activation of carbide-derived carbon, Carbon 49 [11] (2011) 3679–3686.
doi: 10.1016/j.carbon.2011.05.003

[21] S.H. Yeon, P. Reddington, Y. Gogotsi, J.E. Fischer, C. Vakifahmetoglu, P. Colombo, Carbide-derived-carbons with hierarchical porosity from a preceramic polymer, Carbon 48 [1] (2010) 201–210.
doi: 10.1016/j.carbon.2009.09.004

[22] C. Vakifahmetoglu, V. Presser, S.H. Yeon, P. Colombo, Y. Gogotsi, Enhanced hydrogen and methane gas storage of silicon oxycarbide derived carbon, Microp. Mesop. Mater. 144 (2011) 105–112.
doi: 10.1016/j.micromeso.2011.03.042

[23] S. Ishikawa, T. Saito, K. Kuwahara, Carbon Materials with Nano-sized Pores Derived from Carbides, SEI Tech. Review (2016) 152–157.

[24] L. Chen, G. Behlau, Y. Gogotsi, M.J. McNallan, Carbide derived carbon (CDC) coatings for Tyranno ZMI SiC fibers, Ceram. Eng. Sci. Proc. 24 (2003) 57–62. doi: 10.1002/9780470294802.ch8

[25] A. Delcamp, L. Maille, B. Rufino, S. Mazerat, R. Pailler, A. Guette et al. In-situ processing of carbon coating on the surface of SiC-based fibers, Surf. Coat. Tech. 205 [3] (2010) 703–739. doi: 10.1016/j.surfcoat.2010.07.060

[26] Delcamp A. Protection de fibres base SiC pour composites à matrice céramique, University of Bordeaux France, PhD thesis, 2008.

[27] L. Chen, Carbothermal synthesis of coatings on SiC fibers, PhD thesis, University of Drexel, 2004.

[28] S. Mazerat S, Fibres de renfort pour composites SiC/SiC : amélioration et corrélation de la durée de vie sous air à T<900°C avec la réactivité chimique, University Bordeaux France, PhD thesis, 2012.

[29] S. Mazerat, G. Puyoo, G. Chollon, F. Teyssandier, R. Pailler, S. Loison, E. Philippe, Composition and reactivity of various silicon carbide fibers, HTCMC8 Ceram. Trans. 248 (2014) 113–123. doi: 10.1002/9781118932995.ch13

[30] M. Brisebourg, S. Mazerat, G. Puyoo, H. Plaisantin, P. Dibandjo, G.D. Soraru et al. Si-C-O fibres in gas reactive atmospheres, Adv. Sci. Tech. 71 (2010) 86–91. doi: 10.4028/www.scientific.net/AST.71.86

[31] S. Mazerat, J. Lacroix, B. Rufino, R. Pailler, Carbon derived from silicon carbide fibers, a comparative study, Mat. Today Comm. 19 (2019) 177–185. doi: 10.1016/j.mtcomm.2019.01.013

[32] S. Mazerat, A. Delcamp, R. Pailler, J. Lamon, H. Plaisantin, Improvement of silicon carbide fibers mechanical properties by Cl_2 etching, J. Eur. Ceram. Soc. 38 [16] (2018) 5301–5310. doi: 10.1016/j.jeurceramsoc.2018.06.026

[33] A. Delcamp, L. Maille, S. Saint Martin, R. Pailler, A. Guette, Al-O-N and Al-O-B-N thin films applied on Si-O-C fibers, Comp. Sci. Technol. 70 [4] (2010) 622–626. doi: 10.1016/j.compscitech.2009.12.012

[34] L. Chen, H. Ye, Y. Gogotsi, Carbothermal synthesis of boron nitride coatings on silicon carbide, J. Am. Ceram. Soc. 86 [11] (2003) 1830–1837. doi: 10.1111/j.1151-2916.2003.tb03568.x

[35] L. Chen, H. Ye, Y. Gogotsi, Structure of nanocrystalline BN and BN/C coatings on SiC, Proc. Nanostr. Mater. Nanotechnol. 148 (2004) 109–119. doi: 10.1002/9781118406083.ch1

[36] S. Mazerat, R. Pailler, Self organized nano-scale multilayer coating by phosphating SiC fibers, J. Eur. Ceram. Soc. 38 [6] (2018) 2486–2494. doi: 10.1016/j.jeurceramsoc.2017.12.036

[37] T.Y. Tien, F.A. Hummel, The system SiO_2-P_2O_5, J. Am. Ceram. Soc. 45 (1962) 422–424. doi: 10.1111/j.1151-2916.1962.tb11186.x

[38] T. Saeki, E. Narita, H. Naito, Kinetic study on hydrolysis of silicon phosphate in aqueous alkaline solutions, Chem. Soc. Jpn. 57 (1984) 1591–1595. doi: 10.1246/bcsj.57.1591

[39] M.J.B Evans, E Halliop, J.A.F MacDonald, The production of chemically-activated carbon, Carbon 37 [2] (1999) 269–274. doi: 10.1016/S0008-6223(98)00174-2

[40] S.Y. Moon, M.S. Kim, H.S. Hahm, Y.S. Lim, Preparation of activated carbon fibers by chemical activation method with hydroxides, Mat. Sci. Forum 510–511 (2006) 750–753. doi:10.4028/www.scientific.net/MSF.510-511.750

[41] M. Sevilla, R. Mokaya, Energy storage applications of activated carbons: supercapacitors and hydrogen storage, Ener. Environmental Sci. 7 [4] (2014) 1250–1280.

doi: 10.1039/c3ee43525c.

[42] A. Linares-Solano, M.A. Lillo-Ródenas, J.P. Marco-Lozar, M. Kunowsky, A.J. Romero-Anaya, NaOH and KOH for preparing activated carbons used in energy and environmental applications, Int. J. Energy, Env. Eco. 20 [4] (2012) 59–91.

[43] J. Laine, A.Calafat, M.labady, Preparation and characterization of activated carbons from coconut shell impregnated with phosphoric acid, Carbon 27 [2] (1989) 191–195.
doi: 10.1016/0008-6223(89)90123-1

[44] M. Molina-Sabio, F. RodRíguez-Reinoso, F. Caturla, M.J. Sellés, Porosity in granular carbons activated with phosphoric acid, Carbon 33 [8] (1995) 1105–1113.
doi: 10.1016/0008-6223(95)00059-M

[45] L. Wang, Y. Guo, B. Zou, C. Rong, X. Ma, Y. Qu, Y. Li and Z. Wang, High surface area porous carbons prepared from hydrochars by phosphoric acid activation, Biores. Technol. 102 (2011) 1947–1950.
doi: 10.1016/j.biortech.2010.08.100

[46] S. Yajima, M. Omori, J. Hayashi, K. Okamura, T. Matsuzawa, C.F. Liaw, Simple synthesis of the continuous SiC fiber with high tensile strength, Chem. Let. (1976) 551–554.
doi: 10.1246/cl.1976.551

[47] A. R. Bunsell, A. Piant, A review of the development of three generations of small diameter silicon carbide fibres, J. Mater. Sci. 41 (2006) 823–839.
doi: 10.1007/s10853-006-6566-z

[48] F. Teyssandier, G. Puyoo, S. Mazerat, G. Chollon, R. Pailler, F. Babonneau, Contribution to the understanding of the microstructure of first generation Si–C–O fibers, Ceram. Eng. Sci. Proc. 33 [8] (2013) 1–10.
doi: 10.1002/9781118217528.ch1

[49] S. Brunauer, P.H. Emmett, E. Teller, Adsorption of gases in multimolecular layers, J. Am. Chem. Soc. 60 (1938) 309–319.
doi: 10.1021/ja01269a023

[50] G. Horvath, K. Kawazoe, Method for the calculation of effective pore size distribution in molecular sieve carbon, J. Chem. Eng. Jpn. 16 [6] (1983) 470–475.
doi: 10.1252/jcej.16.470

[51] E.P. Barrett, L.G. Joyner, P.P. Halenda, The determination of pore volume and area distributions in porous substances. I. Computations from nitrogen isotherms, J. Am. Chem. Soc. 73 (1951) 373–380.
doi: 10.1021/ja01145a126

[52] K.S.W. Sing, D.H. Everett, R.A.W. Haul, L. Moscou, R.A. Pierotti, J. Rouquerol et al. Reporting physisorption data for gas/solid systems, Pure. App. Chem. 57 [4] (1985) 603–619.

doi: 10.1351/pac198254112201

[53] M. Thommes, K. Kaneko, A.V. Neimark, J.P. Olivier, F.R. Reinoso, J. Rouquerol et al. Physisorption of gases, with special reference to the evaluation of surface area and pore size distribution (IUPAC Technical Report), Pure App. Chem. 87 (2015).
doi: 10.1515/pac-2014-1117

[54] R. Youngman, C. Hogue, B. Aitken, Crystallization of silicon pyrophosphate from silicophosphate glasses as monitored by multi-nuclear NMR, Mat. Res. Soc. Proc. (2006) 984.
doi: 10.1557/PROC-984-0984-MM12-03

[55] S. Sakida, T. Nanba, Y. Miura, Structural change around Si atoms in P_2O_5-SiO_2 binary glasses before and after annealing by ^{29}Si MAS NMR Spectroscopy, Chem. Lett. 35 [11] (2006) 1268–1269.
doi: 10.1246/cl.2006.1268

[56] M. Thommes, Physical Adsorption Characterization of Nanoporous Materials, Chem. Ing. Tech. 82 [7] (2010) 1059–1073.
doi: 10.1002/cite.201000064

[57] I.W. Smith, The intrinsic reactivity of carbons to oxygen, Fuel 57 (1978) 409–414.
doi: 10.1016/0016-2361(78)90055-8

[58] S.R. Choi, J.P. Gyekenyesi, Crack branching and fracture mirror data of glasses and advanced ceramics, NASA, 206536 (1998) 1–19.

[59] S.T. Taylor, Y.T. Zhu, W.R. Blumenthal, M.G. Stout, D.P. Butt, T.C. Lowe, Characterization of Nicalon fibres with varying diameters part I strength and fracture studies, J. Mater. Sci. 33 (1998) 1465–1473.
doi: 10.1023/A:1004343608115

[60] T. Morimoto, S. Nakagawa, S. Ogihara, Bias in the Weibull strength estimation of a SiC fiber for the small gauge length case, Jap. Soc. Mech. Eng. 48 (2005) 194–198.
doi: 10.1023/A:1018600119250

[61] Y. Gogotsi, A. Nikitin, H. Ye, W. Zhou, J.E. Fisher, B. Yi. et al. Nanoporous carbide-derived carbon with tunable pore size, Nature Mat. 2 (2003) 591–594.
doi: 10.1038/nmat957

[62] J.C. Groen, L.A.A. Peffer, J. Pérez-Ramírez, Pore size determination in modified micro- and mesoporous materials. Pitfalls and limitations in gas adsorption data analysis, Microp. Mesop. Mater. 60 (2003) 1–17.
doi: 10.1016/S1387-1811(03)00339-1

[63] Osswald S, Portet C, Gogotsi Y, Laudisio G, Singer JP, Fischer JE, et al. Porosity control in nanoporous carbide-derived carbon by oxidation in air and carbon dioxide, J. Solid State Chem. 182 (2009) 1733–1741.

doi: 10.1016/j.jssc.2009.04.017

Graphical abstract

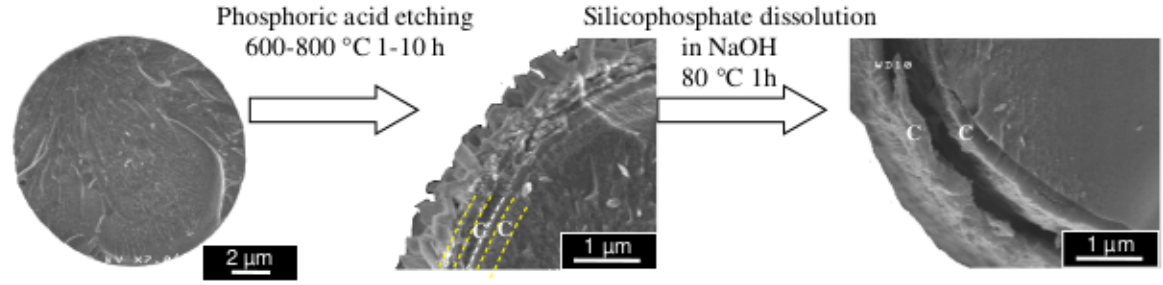

SiC-based fiber

Surface transformation into
$(C/silicophosphate)_n$ coating

Shaped carbide
derived carbon